EUROPEAN ORGANIZATION FOR NUCLEAR RESEARCH
European Laboratory for Particle Physics

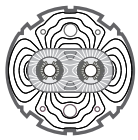

Large Hadron Collider Project

LHC Project Report 180

The Electron-Cloud Effect in the Arcs of the LHC[‡,§]

Miguel A. Furman[*,†]

Abstract

We present an update of our estimates for the power deposition arising from the electron-cloud effect in the dipole bending magnets in the arcs of the LHC. In addition, we present the estimate of the power deposition in the field-free regions in the arcs. We hold the number of particles per bunch and the bunch spacing fixed at their nominal values, and we assume throughout a high photon reflectivity. We explore the dependence of the power deposition on the photoelectric efficiency and on secondary emission yield parameters. We find a marked sensitivity to parameters that characterize secondary emission on the scale of $5 - 10$ eV.

[*]Member of the US collaboration to the LHC project.
[†]MAFurman@lbl.gov. Center for Beam Physics, Lawrence Berkeley National Laboratory, Berkeley, CA 94720, USA.
[‡]Work supported by the US Department of Energy under contract no. DE-AC03-76SF00098.
[§]Also published as LBNL-41482/CBP Note 247.

Administrative Secretariat
LHC Division
CERN
CH-1211 Geneva 23
Switzerland

Geneva, May 20, 1998

Contents

List of Figures

List of Tables

1 Introduction.

The electron-cloud effect (ECE) for the LHC has been actively investigated for this past year, particularly concerning the energy deposition by the electrons on the walls of the beam screen [1–10]. In this note we present an update of our calculations for the power deposition arising from the ECE in the dipole bending magnets in the arcs of the LHC, whose preliminary results were reported in Ref. 3. In addition, we estimate here the power deposition in the field-free regions in the arcs.

In all results presented here we assume that the photon reflectivity R is close to unity. Simple geometrical arguments indicate that lower values of R imply lower values for the power deposition in the dipole magnets. However, a detailed calculation for low R is much more involved, and we intend to carry it out separately. We explore here the dependence of the power deposition on other parameters such as the quantum efficiency Y', the characteristic energy E_{ph} and width σ_{ph} of the photoelectron distribution, the peak value of the secondary emission yield (SEY) $\hat{\delta}$, and the characteristic energy of the emitted secondary electrons E_s. Other parameters, such as beam energy, number of particles per bunch, bunch spacing, etc., are held fixed at their nominal values. We neglect electrons generated by ionization of the residual gas because, for typical parameters, they constitute a negligible source compared to photoemission [11].

The main changes relative to our preliminary report are the following: (a) we now discount those photons whose energy is less than the work function of the surface; (b) for the purposes of facilitating a comparison with results presented in Ref. 10, we now ignore the elastically-backscattered and rediffused components of the SEY (we comment on this particular approximation in Sec. 10.5); (c) we have updated certain parameters of the SEY so as to better represent the data for copper; and (d) we now fully include bunch length effects. In addition, we now use a better approximation for the electric field produced by the bunch, so that it represents the true field of a gaussian charge distribution and it also satisfies the perfect-conductor boundary condition on the surface of the beam screen.

For the specific values $Y' = 0.2$, $\hat{\delta} = 1.3$ and $E_s = 5$ eV, our present estimate of the power deposition per unit length in the dipole magnets and in the field-free regions of the arcs is ~ 0.75 W/m and ~ 4 W/m respectively. The value 0.75 W/m for the dipole magnets is more than a factor of 6 below our preliminary estimate [3]. Items (a) and (b) above contribute more than a factor of 2 each to the decrease of the estimate, and items (c) and (d) together roughly contribute an additional 50%. It turns out that, although our new expression for the electric field is physically more satisfactory than the linearized approximation we used earlier, the change has the effect of lowering the estimate of the power deposition by only $\sim 10\%$.

The power deposition is sensitive to details of the secondary emission process at low energies, in the range $5 - 10$ eV. Thus, if one assumes $E_s = 10$ eV instead of 5 eV, the power deposition per unit length in the dipoles is reduced by roughly 50%. Similarly, if one includes the elastic and rediffused components of the SEY at fixed $E_s = 5$ eV, the estimate for the power deposition increases by roughly 150%. The physical origin of this sensitivity [9, 10, 12] is the fact that the minimum energy required by an electron to cross the beam screen in one bunch spacing (25 ns), which is 6 eV, is in the mid-range of values we consider for E_s. Electrons slower than this get kicked by more than one bunch, leading to a substantially higher collision energy, and hence power deposition, on the walls of the beam screen. On the other hand, the power deposition is not very sensitive to details of the photoelectron energy distribution parameters in the range $5 - 10$ eV. We attribute

this fact to bunch-length effects.

Our results are in good agreement with those in Ref. 10 for those cases in which a comparison is meaningful. This agreement strengthens our confidence in the methods used to simulate the ECE, and re-emphasizes the relevance of low-energy secondary emission parameters for the power deposition in the LHC beam screen. It is important, therefore, to pin down these parameters so that a more reliable estimation of the power deposition can be obtained from our simulations.

2 Machine model.

For the purpose of studying the electron-cloud effect we use a simplified model to represent the beam, the beam screen and the elements of the arcs [3]. Here is a brief summary, in the interest of completeness: The beam is assumed to be composed of identical, evenly-spaced bunches separated by $s_B = 7.48$ m; there are no gaps in the bunch train. We assume a bunch population $N_p = 1.05 \times 10^{11}$ protons per bunch, average transverse rms beam sizes $\sigma_x = \sigma_y = 0.3$ mm and rms bunch length $\sigma_z = 7.7$ cm.

We represent the cross-section of the beam screen [13] by an ellipse with semiaxes $a = 2.2$ cm and $b = 1.8$ cm, as sketched in Fig. 1. This approximation allows us to use the exact formula for the electric field produced by the beam and by the space charge of the electrons in the cloud [14].

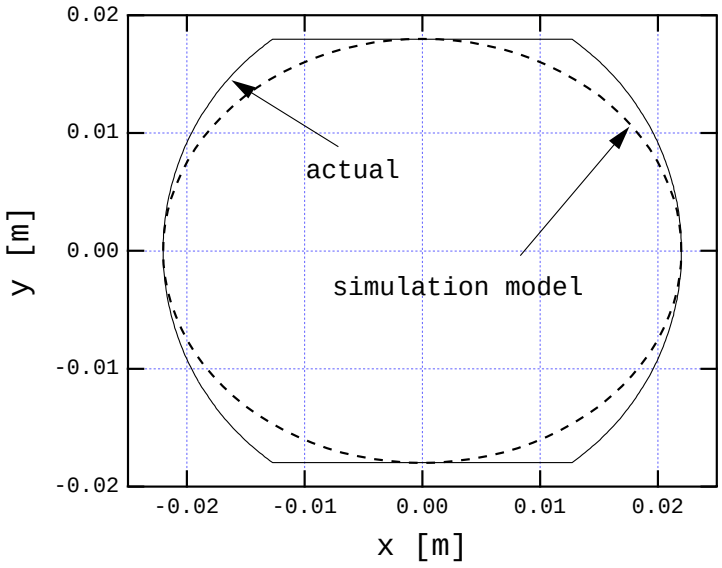

Figure 1: In our model, we replace the actual transverse cross-section of the beam screen by the inscribed ellipse.

We assume that the "ring" consists of 1232 identical, evenly-spaced dipole bending magnets of length 14.2 m and 1232 field-free sections of length 7.44 m in between every pair of dipole magnets. The basic periodic unit of this model ring therefore has a length $L_u = 14.2 + 7.44 = 21.64$ m. These lengths add up to a circumference of 26660.48 m. The dipoles have a magnetic field $B = 8.4$ T, and the beam orbit through them has a radius of curvature $\rho = 2784.32$ m. The section of arc subtended by a dipole magnet is $\Delta\theta = 2\pi/1232 = 5.1 \times 10^{-3}$ rad.

3 Photoelectron emission.

For a beam energy $E = 7$ TeV, the critical energy of the synchrotron radiation from a proton traversing a dipole magnet is given by

$$E_{\rm crit} = \frac{3\hbar c}{2\rho}\,\gamma^3 = 44.1 \text{ eV} \tag{1}$$

where γ is the usual relativistic factor. Each proton generates, on average,

$$N_{\gamma/p,\rm tot} = \frac{5\alpha\gamma}{2\sqrt{3}}\,\Delta\theta = 0.4 \tag{2}$$

incoherent photons of all energies and directions upon traversing any given dipole bending magnet, where $\alpha \simeq 1/137$ is the fine structure constant (coherent photons can be completely neglected due to their very low energy). Those photons whose energy is below the work function of the metal do not yield photoelectrons. The fraction of photons whose energy E_γ is below a cut-off value $E_{\rm cut} < E_{\rm crit}$ is

$$\frac{\Delta N_{\gamma/p,\rm tot}(E_\gamma \le E_{\rm cut})}{N_{\gamma/p,\rm tot}} \simeq \frac{3^{3/2}2^{5/3}}{5\Gamma(1/3)}\left(\frac{E_{\rm cut}}{E_{\rm crit}}\right)^{1/3} = 0.55 \tag{3}$$

where the numerical value 0.55 corresponds to $E_{\rm cut} = 4$ eV, which we assume to be the value of the work function. Therefore only 45% of the 0.4 emitted photons contribute to photoproduction. Table 1 summarizes the relevant parameter values.

Table 1: LHC synchrotron radiation parameters.

Beam energy, E [TeV]	7
Relativistic factor, γ	7460.52
Dipole magnet field, B [Tesla]	8.4
Dipole magnet length, L_B [m]	14.2
Bending radius, ρ [m]	2784.32
Dipole magnet arc section, $\Delta\theta$ [mrad]	5.1
Critical energy, $E_{\rm crit}$ [eV]	44.1
No. of radiated photons per proton, $N_{\gamma/p,\rm tot}$	0.4
No. of radiated photons per proton above 4 eV, $N_{\gamma/p}$	0.18

If Y is the number of photoelectrons generated per incident photon and Y' the number of photoelectrons generated per absorbed photon, then [3, 7, 11]

$$Y' = \frac{Y}{1-R} \tag{4}$$

where R is the photon reflectivity. The parameter Y has an implicit dependence on R such that $Y \to 0$ when $R \to 1$. Assuming that the photon reflection is specular and that fluorescence can be ignored, it is straightforward to show that the quantity Y' represents the total number of photoelectrons per emitted photon that are generated *anywhere at any time* downstream of the emission point [3, 11].

3.1 Average number of photoelectrons generated per bunch passage.

If $R \lesssim 1$, the photons bounce many times inside the chamber downstream of their emission point and, as a result, they get distributed quite uniformly both longitudinally (along the pipe) and transversely before they yield photoelectrons. As a result, the photoelectrons are also generated approximately uniformly. In a section of the vacuum chamber of length L the time-averaged number of photoelectrons generated in a time interval equal to the bunch spacing, s_B/c following the passage of a single bunch through a bending magnet is [11]

$$\bar{N}_e = Y' N_{\gamma/p} N_p \frac{L}{L_u} \tag{5}$$

where Y' represents here, and in the rest of this note, an effective yield, *i.e.*, an average over the photon spectrum.

When $R \simeq 0$ the photons essentially do not bounce in the chamber, and therefore yield photoelectrons (or get absorbed) upon first strike. In this case the distribution of photoelectrons is far from uniform, and a proper calculation requires a detailed integration of the photon spectrum folded with the geometry of the vacuum chamber. We have not yet carried out such calculation, and will not consider this case any further in this note. However, it is clear that the largest power deposition from the electron cloud in the dipole magnets increases with R, hence our calculation for $R \lesssim 1$ represents an upper limit.

3.2 Distribution in position and momentum of the photoelectrons.

Since $R \lesssim 1$ we assume that the photoelectrons are generated on the surface of the elliptical beam screen with distribution

$$\frac{dN}{ds d\zeta} \propto \sqrt{x^2 + y^2} \tag{6}$$

where x and y are the transverse coordinates of the point of photoemission on the surface of the beam screen, s is the longitudinal position along the pipe, and ζ is the elliptical coordinate of the point (x, y), defined by the equations

$$x = a \cos\zeta, \quad y = b \sin\zeta \tag{7}$$

The distribution (6) implies that the number of photoelectrons emitted per unit beam screen area is $\propto a/b$ for $(x, y) = (\pm a, 0)$ and $\propto b/a$ for $(x, y) = (0, \pm b)$. Thus our choice (6) emphasizes the horizontal "corners" of the ellipse, which seems physically reasonable.

The distribution in energy and angles is assumed of the form

$$\frac{dN}{dE d\theta d\phi} \propto \theta(E)\, e^{-(E-E_{ph})^2/2\sigma_{ph}^2} \cos\theta \tag{8}$$

where θ and ϕ are the polar and azimuthal angles relative to the normal to the surface at the emission point and the step function $\theta(E)$ ensures the positivity of the kinetic energy E. In most simulations presented here we choose $E_{ph} = \sigma_{ph} = 5$ eV.

3.3 Time structure of the photoelectrons.

As mentioned above, $\bar{N}_e$ represents a time-averaged the number of photoelectrons. The simulation of the electron-cloud effect, on the other hand, requires the spatial and temporal details of the photoemission process. When the beam traverses a dipole bending

magnet, the generated photons have the same time structure as the beam. In particular, if the bunch has a gaussian longitudinal charge density with rms length σ_z, so does the pulse of photons generated by this bunch. If the photon reflectivity is specular and if $R \sim 1$, the photon pulse travels approximately together with the proton bunch even after bouncing several times off the chamber walls. Thus the photoelectrons are produced concurrently with the bunch as it traverses any given section of the chamber. Since the photoelectric process is probabilistic, a given photoelectron may experience the full kick from the bunch if it is generated at the head of the pulse, or a small fraction of the kick if it is generated at the tail. For a longitudinal gaussian distribution the beam kick experienced by a photoelectron upon being generated is weighted by the factor

$$\int_{t_{cr}}^{\infty} dt \hat{\lambda}(t) = \frac{1}{2}\left(1 - \mathrm{erf}\left(\frac{t_{cr}}{\sqrt{2}\sigma_t}\right)\right) \tag{9}$$

where t_{cr} is the creation time of the photoelectron relative to the instant of passage of the center of the bunch, $\hat{\lambda}(t)$ is the normalized longitudinal charge distribution of the bunch as a function of time t, and $\sigma_t = \sigma_z/c$. Of course, these electrons will sample the entire length of the bunch from successive bunches.

4 Secondary emission process.

The generally-accepted picture of secondary emission [15] is the following: when a current I_0 of electrons strikes the surface of a material, a certain portion I_e is elastically backscattered off the surface, and the rest penetrates into the material. Some of these electrons scatter from one or more atoms and are reflected back out (these are the so-called "rediffused" electrons), yielding a current I_r. The rest of the electrons interact in an inelastic way with the material and yield a current I_{ts} of "true secondary" electrons.

Our complete model of the SEY is presented in Ref. 11. However, for the purpose of facilitating a comparison with Ref. 10, in this report we mostly neglect the backscattered and rediffused components of the SEY, and consider only the true secondary yield $\delta_{ts} = I_{ts}/I_0$, *i.e.*, we set $\delta = \delta_{ts}$. We now summarize this simplified model.

The traditional quantities that describe secondary emission are the yield $\delta(E_0, \theta_0)$ and its dependence on the emitted energy, $d\delta/dE$. In these expressions E_0 and θ_0 are the incident kinetic energy of the electron and its angle relative to the normal to the surface at the point of impact, and E is the aggregate energy of the emitted secondaries. The simulation, however, requires more information than these two average quantities because it needs to know, on an event-by-event basis, the number of emitted secondary electrons, their energies and angles. The mathematical objects that contain all the information relevant to the process are the "most differential" probabilities

$$\mathcal{P}_n \equiv \frac{dP_n}{dE_1 d\Omega_1 dE_2 d\Omega_2 \cdots dE_n d\Omega_n}, \quad n = 1, 2 \cdots \tag{10}$$

for the emission of n electrons. Here E_k and $\Omega_k = (\theta_k, \phi_k)$ are the kinetic energy and solid angle of the k-th ejected electron, respectively. Our simulation code POSINST embodies a model for the $\mathcal{P}_n$'s, described below, that is consistent with measured values of δ and $d\delta/dE$. Obviously such a model is far from unique.

The probability that n electrons will be emitted with arbitrary energies and directions for a fixed incident angle and energy, $P_n(E_0, \theta_0)$, is obtained by integrating (10) over

the entire phase space of the secondary electrons,

$$P_n(E_0, \theta_0) = \int (dE)_n (d\Omega)_n \, \mathcal{P}_n \tag{11}$$

where the symbols $(dE)_n$ and $(d\Omega)_n$ are the n-body volumes of kinetic energy and solid angle, respectively, $(dE)_n \equiv dE_1 dE_2 \cdots dE_n$ and $(d\Omega)_n \equiv d\Omega_1 d\Omega_2 \cdots d\Omega_n$. The P_n's must obey the conditions

$$P_n \geq 0, \;\; n = 0,\, 1,\, 2,\, \cdots \qquad \text{and} \quad \sum_{n=0}^{\infty} P_n = 1 \tag{12}$$

where P_0 is the probability that the incident electron is absorbed without the emission of any electrons. The SEY is the average electron multiplicity,

$$\delta(E_0, \theta_0) = \langle n \rangle \equiv \sum_{n=1}^{\infty} n P_n \tag{13}$$

and $d\delta/dE$ is given by[1)]

$$\frac{d\delta}{dE} = \sum_{n=1}^{\infty} n \int (dE)_n (d\Omega)_n \, \mathcal{P}_n \, \delta(E - E_1 - E_2 - \cdots - E_n) \tag{14}$$

This equation yields δ upon integration over E from 0 to ∞, as it should. Eqs. (11–14), along with the requirement of energy conservation, provide the basic constraints to construct the model for the $\mathcal{P}_n$'s.

4.1 Dependence on incident energy and angle.

The energy and angular dependence of δ are usually well fit experimentally by a scaling function $D(x)$ [15, 16],

$$\delta(E_0, \theta_0) = \hat{\delta}(\theta_0) D(E_0/\hat{E}(\theta_0)) \tag{15}$$

so that all dependence on the surface and incident angle θ_0 is contained in $\hat{\delta}$ and $\hat{E}$. The scaling function $D(x)$ is defined so that it satisfies the conditions $D(1) = 1$ and $D'(1) = 0$, which are, of course, chosen to ensure that δ reaches a peak value $\hat{\delta}$ at an energy $E_0 = \hat{E}$.

The function $D(x)$ is approximately a universal curve. For our purposes, we have chosen the simplest form that satisfies the above-mentioned conditions and that allows a good fit to the data namely

$$D(x) = \frac{sx}{s - 1 + x^s} \tag{16}$$

where the parameter s must be > 1. This function is shown in Fig 2.

Measurements at SLAC show that data for aluminum at normal incidence is well fit by $s = 1.44$. The experimental measurements for incidence away from normal [17] both for aluminum and TiN demand that all three parameters $\hat{\delta}$, $\hat{E}$ and s depend on the incident angle θ_0 [17]. For smooth surfaces, the incident-angle dependence of $\hat{\delta}$ and $\hat{E}$ is usually well parametrized by a power law of the form $\hat{\delta}(\theta_0) \propto (\cos\theta_0)^{-q}$ and $\hat{E}(\theta_0) \propto (\cos\theta_0)^{-r}$, where θ_0 is measured relative to the normal to the surface [16]. For technical surfaces,

[1)] Dirac's δ, appearing in the integrand, should not be confused with the SEY.

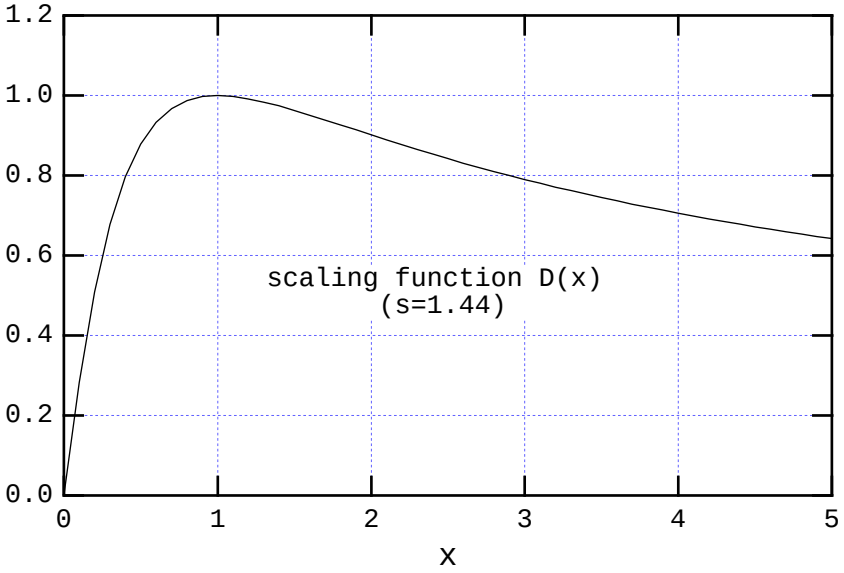

Figure 2: The scaling function $D(x)$, Eq. (16), for $s = 1.44$.

such as the PEP-II vacuum chamber even after TiN coating [17], we have found that these parametrizations are inadequate. A better fit is obtained with

$$s(\theta_0) = s(0) \times (1 - 0.18(1 - \cos\theta_0)) \tag{17a}$$

$$\hat{E}(\theta_0) = \hat{E}(0) \times (1 + 0.7(1 - \cos\theta_0)) \tag{17b}$$

$$\hat{\delta}(\theta_0) = \hat{\delta}(0) \times (1 + 0.26(1 - \cos^2\theta_0)) \tag{17c}$$

The numerical constants appearing in Eq. (17), including the powers of $\cos\theta_0$, are only approximate, and were obtained from the incident-angle dependence measurements for an uncoated aluminum sample. We assume here that the same numerical constants will describe the copper-coated LHC beam screen, for which we also assume $\hat{E}(0) = 400$ eV and $\hat{\delta}(0) = 1.3$, although we will present results for other values in the range $0 \le \hat{\delta}(0) \le 1.8$. Figure 3 shows curves of the SEY of copper for the above-mentioned parameters.

4.2 Energy and angle dependence of emitted electrons.

The true secondary electrons emitted from amorphous surfaces have an approximate $\cos\theta$-distribution in angle, which is fairly independent of the incident angle θ_0. Thus we assume the simplest uncorrelated form for $\mathcal{P}_n$,

$$\mathcal{P}_n = \frac{dP_n}{(dE)_n} \times \frac{\cos\theta_1 \cos\theta_2 \cdots \cos\theta_n}{\pi^n} \tag{18}$$

where the emission angles θ_k are measured relative to the normal to the surface at the collision point. The normalization factor $1/\pi^n$ ensures that the integral $\int (d\Omega)_n$ over the hemisphere away from the surface is unity.

Next we make the assumption that, for $n \ge 1$, $dP_n/(dE)_n$ is of the form

$$\frac{dP_n}{(dE)_n} = f_n(E_1) f_n(E_2) \cdots f_n(E_n)\, \theta(E_0 - E_1 - E_2 - \cdots - E_n) \tag{19}$$

where the f_n's are the single-electron kinetic energy distributions. This expression implies that the electrons are emitted almost independently of each other; the only constraint that

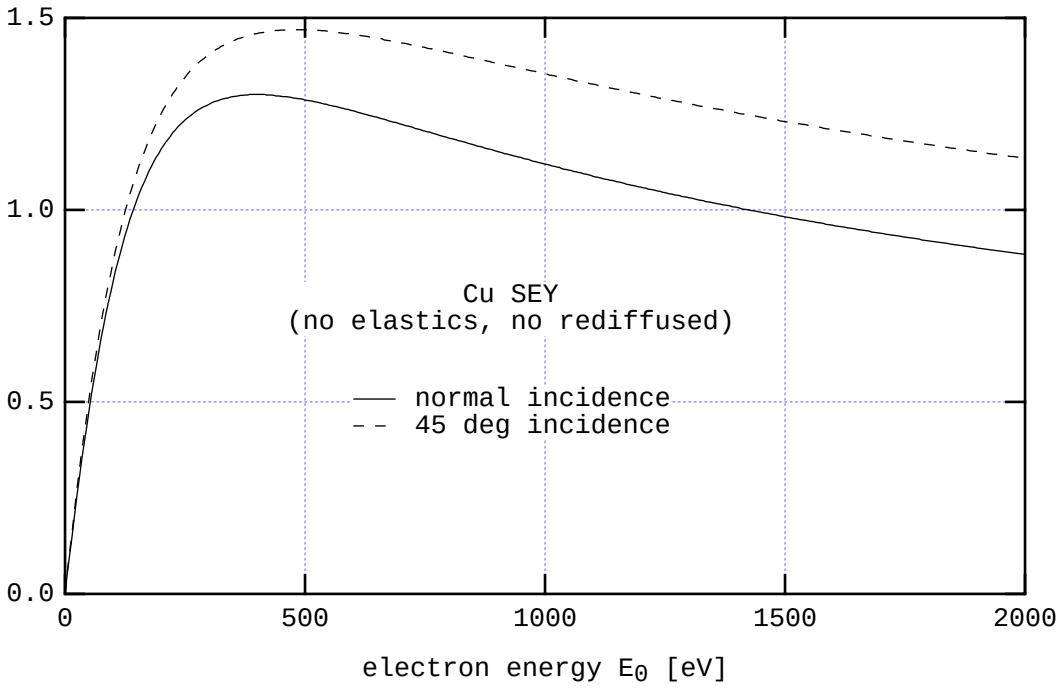

Figure 3: SEY for copper obtained from our model, Eqs. (16) and (17), with $\hat{\delta}(0) = 1.3$, $\hat{E}(0) = 400$ eV and $s(0) = 1.44$.

they must collectively obey, which is enforced by the θ-function, is that their aggregate energy should not exceed the primary electron energy E_0. The explicit form assumed for f_n is

$$f_n(E, E_0, \theta_0) = F_n(E_0, \theta_0)\, E^{p-1} e^{-E/E_s}, \quad n \geq 1 \tag{20}$$

For our simulations we choose $p = 2$, which appears to be consistent with measurements of various materials [15, 18, 19]. For the specific parameter regime of the LHC, there is an important dependence on the parameter E_s, and we shall present results for $E_s = 5$ and 10 eV.

The quantity F_n appearing in f_n is related to P_n *via* the integral

$$\begin{aligned} P_n &= \int_0^\infty (dE)_n\, f_n(E_1) f_n(E_2) \cdots f_n(E_n)\, \theta(E_0 - E_1 - E_2 - \cdots - E_n) \\ &= \frac{(E_s^p \Gamma(p) F_n)^n\, \gamma(np, E_0/E_s)}{\Gamma(np)} \end{aligned} \tag{21}$$

where $\gamma(z, x)$ is the incomplete gamma function [20]. The final ingredient in the definition of the model is the connection between P_n and δ. For this we assume a simple Poisson distribution,

$$P_n(E_0) = \frac{\delta^n}{n!} e^{-\delta}, \ n \geq 1 \tag{22}$$

which has a mean $\langle n \rangle = \delta$, as it should in order for δ to have the required meaning of being the average number of secondary electrons. The probability P_0 that an incident electron gets absorbed with no electrons generated is determined from Eq. (12),

$$P_0 = 1 - \sum_{n=1}^{\infty} P_n = e^{-\delta} \tag{23}$$

4.3 Algorithm for the secondary emission process.

With all these ingredients, we can now state the algorithm used by POSINST for the secondary emission process when an electron hits the chamber wall:

1. Record the point of impact and compute the inward unit vector normal to the surface, $\hat{\mathbf{n}}$.
2. Record the incident energy E_0 and angle θ_0 relative to $\hat{\mathbf{n}}$.
3. Compute δ according to Eq. (15), including the angular dependence factors in Eq. (17).
4. Compute the probabilities P_n for $n = 1,\ 2,\ \cdots,\ 10$ according to Eq. (22) and P_0 according to Eq. (23).
5. Generate a random integer $m \in \{0,\ 1,\ \cdots,\ 10\}$ with probability distribution $\{P_0,\ P_1,\ \cdots,\ P_{10}\}$. This is the number of secondary electrons emitted.[2)]
6. If $m = 0$, the incident electron is absorbed without emission; proceed with the next electron.
7. If $m \neq 0$, generate m random polar angles $\theta_k \in (0, \pi/2)$ with probability distribution $\cos\theta$, and m random azimuthal angles $\phi_k \in (0, 2\pi)$ with uniform probability distribution. These angles determine the directions of the m emitted electrons relative to the normal at the surface.
8. Generate m random kinetic energies $E_k \in (0, E_0)$ with probability density $E^{p-1}e^{-E/E_s}$ subject to the constraint $E_1 + \cdots + E_m \leq E_0$. These are the chosen energies for the secondary electrons.

4.4 Energy distribution of secondaries.

It is straightforward to compute $d\delta/dE$ from Eq. (14); we obtain

$$\frac{d\delta}{dE} = \theta(E_0 - E)\left[\frac{1}{E_s}\exp(-\delta - E/E_s)\sum_{n=1}^{\infty}\frac{\delta^n\,(E/E_s)^{np-1}}{(n-1)!\,\gamma(np, E_0/E_s)}\right] \tag{24}$$

which is illustrated in Fig. 4. This curve is consistent with measured data except when $E \lesssim E_0$, where the elastically backscattered electrons lead to a peak in $d\delta/dE$.

5 The transverse electric field.

The electric field produced by the beam in an elliptical, perfectly conducting vacuum chamber is described in detail in Refs. 3 and 11. Here we summarize the expressions and add one improvement.

5.1 Infinitely thin line of charge.

A relativistic charge moving in a straight line produces an electric field that is purely transverse. The transverse electric field per unit line-charge density, which has dimensions of 1/length, is conveniently expressed in complex form,

$$\mathcal{E} = \mathcal{E}_x + i\mathcal{E}_y \tag{25}$$

Consider an elliptical vacuum chamber made of a perfect conductor with semi-axes a and b with $a > b$. Choose the origin of the coordinate system at the center of the ellipse

[2)] We have never seen more than 9 electrons being generated in a single collision.

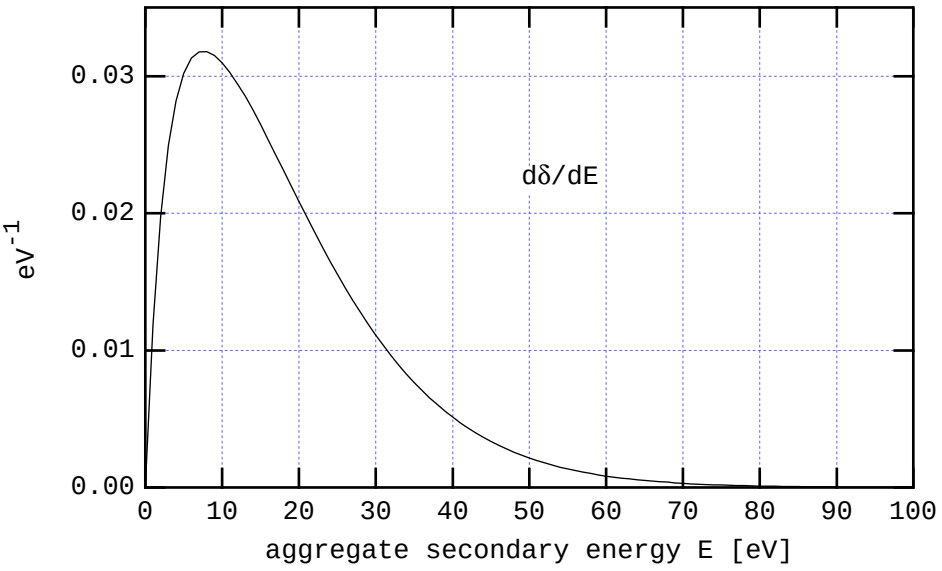

Figure 4: Energy distribution $d\delta/dE$ of emitted secondary electrons for a normally-incident electron with energy $E_0 = 100$ eV. Other parameters are: $\hat{\delta}(0) = 1.3$, $\hat{E}(0) = 400$ eV, $p = 2$, and $E_s = 5$ eV. The backscattered and rediffused components of the SEY are ignored here.

such that the x axis is along a. The problem is solved in elliptic coordinates (μ, ϕ), defined by

$$\left.\begin{aligned} x &= g\cosh\mu\cos\phi \\ y &= g\sinh\mu\sin\phi \end{aligned}\right\} \qquad -\pi < \phi \leq \pi, \quad 0 \leq \mu < \infty \tag{26}$$

The curves with constant μ are confocal ellipses and those with constant ϕ are confocal hyperbolas, the common foci of both families being located at $x = \pm g,\ y = 0$. The solution of Poisson's equation with perfect-conductor boundary conditions [14] requires that g be chosen so that the ellipse that defines the vacuum chamber itself belongs to the family of confocal ellipses. This condition implies that there must be a value $\mu = \mu_c$, which defines the chamber, for which

$$a = g\cosh\mu_c \tag{27a}$$
$$b = g\sinh\mu_c \tag{27b}$$

or, equivalently

$$g = \sqrt{a^2 - b^2} \tag{28a}$$
$$\mu_c = \tanh^{-1}\left(\frac{b}{a}\right) = \frac{1}{2}\log\left(\frac{a+b}{a-b}\right) \tag{28b}$$

If the line of charge is located at a point (x_0, y_0) inside the chamber, the exact expression for the complex electric field is written

$$\mathcal{E} = \mathcal{E}_d + \mathcal{E}_s \tag{29}$$

where the "direct" and "surface" components of the field are given by[3)]

$$\mathcal{E}_d = \frac{2}{\bar{z} - \bar{z}_0} \tag{30a}$$

$$\mathcal{E}_s = \frac{4}{g} \sum_{n=1}^{\infty} e^{-n\mu_c} \left[\frac{\cosh n\mu_0 \cos n\phi_0}{\cosh n\mu_c} + i \frac{\sinh n\mu_0 \sin n\phi_0}{\sinh n\mu_c} \right] \frac{\sinh n\bar{q}}{\sinh \bar{q}} \tag{30b}$$

where $z = x + iy = g \cosh q$ with $q \equiv \mu + i\phi$, and where μ_0 and ϕ_0 are the elliptic coordinates of (x_0, y_0), *i.e.*, $z_0 = x_0 + iy_0 = g \cosh(\mu_0 + i\phi_0)$.

If the line of charge is at the origin, $z_0 = 0$, the expression for $\mathcal{E}_s$ becomes

$$\mathcal{E}_s = \frac{4}{g} \sum_{n=1}^{\infty} \frac{(-1)^n e^{-2n\mu_c}}{\cosh 2n\mu_c} \frac{\sinh 2n\bar{q}}{\sinh \bar{q}} \tag{31}$$

5.2 Round gaussian charge density.

The field produced by a round gaussian charge distribution centered at the origin in free space is given by

$$\mathcal{E}_r = \frac{2}{\bar{z}} \left(1 - e^{-|z|^2/2\sigma^2} \right) \tag{32}$$

where $\sigma_x = \sigma_y \equiv \sigma$. In the usual case when the beam is close to the center of the chamber and its transverse size is small compared with the dimensions of the chamber, $\sigma \ll a, b$, it is possible to write an extremely accurate expression for the field that satisfies the perfect-conductor boundary conditions for the elliptical chamber. The formula is simply

$$\mathcal{E}_{r'} = \mathcal{E}_r + \mathcal{E}_s \tag{33}$$

where $\mathcal{E}_s$ is given by Eq. (31). This is the formula used in all our simulation results presented in this note.

To prove that this expression is approximately correct, we first note that it satisfies the divergence equation *exactly* for a round gaussian charge distribution, since $\mathcal{E}_s$ satisfies the equation with zero source. Now for $|z| \gg \sigma$ the field $\mathcal{E}_r$ approaches $2/\bar{z}$ within a relative accuracy $e^{-(|z|/\sigma)^2/2}$. Therefore $\mathcal{E}_{r'}$ approaches Eqs. (29–30) with a similar accuracy, hence $\mathcal{E}_{r'}$ satisfies the boundary conditions at the surface of the ellipse with an accuracy $\sim e^{-(b/\sigma)^2/2}$, which evaluates to $\simeq 10^{-780}$ for the LHC. This completes the proof.

If the bunch center is at location (x_0, y_0) away from the origin, Eq. (33) must be modified by replacing $(x, y) \to (x - x_0, y - y_0)$ in $\mathcal{E}_r$ and using expression (30b) for $\mathcal{E}_s$; the expression for $\mathcal{E}_{r'}$ remains accurate provided that both $|x_0|$ and $|y_0|$ are $\ll (a, b)$.

Finally, we note that $\mathcal{E}_s \ll \mathcal{E}_r$ near the center of the ellipse. To prove this, we note that, near the origin, Eqs. (31) and (32) yield

$$\mathcal{E}_s = -\frac{8\bar{z}}{g^2} \sum_{n=1}^{\infty} \frac{n e^{-2n\mu_c}}{\cosh 2n\mu_c} + \mathcal{O}(\bar{z}^3) \tag{34a}$$

$$\mathcal{E}_r = \frac{z}{\sigma^2} + \mathcal{O}(z^3) \tag{34b}$$

This implies that in the region $0 \le |z| \lesssim \sigma$ the ratio of the fields is

$$\left| \frac{\mathcal{E}_s}{\mathcal{E}_r} \right| \simeq 16 \left(\frac{\sigma}{g} \right)^2 e^{-4\mu_c} \tag{35}$$

[3)] It should be noted that the n-th term in the summation for the surface field does *not* represent an image charge.

which evaluates to 10^{-4} for LHC parameters. Hence the surface charges have a minor effect near the beam, as one should expect.

5.3 Elliptical gaussian charge density.

In other regions of the machine, *e.g.* in the quadrupole magnets, it may be more correct to assume an elliptical, rather than round, beam charge distribution. We present here, for future reference, the approximate formula for the field that takes into account the elliptic-chamber boundary condition.

If the beam distribution is gaussian with elliptical profile, the previous analysis carries through provided one replaces $\mathcal{E}_r$ by the Bassetti-Erskine [21] formula[4)]

$$\mathcal{E}_{BE} = \frac{2i\sqrt{\pi}}{S}\left[e^{-|\xi|^2/2}\, w\left(\bar{\eta}/S\right) - w\left(\bar{z}/S\right)\right] \tag{36}$$

where $S \equiv (2(\sigma_x^2 - \sigma_y^2))^{1/2}$, $\eta \equiv \sigma_y x/\sigma_x + i\sigma_x y/\sigma_y$, $\xi \equiv x/\sigma_x + iy/\sigma_y$ and $w(z)$ is the complex error function [20]. Thus the approximate expression for the field in the presence of an elliptical perfect conductor is

$$\mathcal{E}_{BE'} = \mathcal{E}_{BE} + \mathcal{E}_s \tag{37}$$

In this case, however, the error with which this expression satisfies the boundary condition, though still small, is much larger than in the round-beam case. This is because, for $|z| \gg \sigma_x, \sigma_y$ and $\sigma_x > \sigma_y$, Eq. (36) implies

$$\mathcal{E}_{BE} = \frac{2}{\bar{z}}\left(1 + \frac{\sigma_x^2 - \sigma_y^2}{\bar{z}^2} + \mathcal{O}\left(\bar{z}^{-4}\right)\right) \tag{38}$$

hence $\mathcal{E}_{BE'}$ fails to satisfy the boundary condition by an amount $\sim (\sigma_x/b)^2 \sim 3 \times 10^{-4}$ rather than by $\sim e^{-(b/\sigma)^2/2} \simeq 10^{-780}$. Again, if the bunch center is at location (x_0, y_0) away from the origin, $\mathcal{E}_{BE'}$ must be modified by replacing $(x, y) \to (x - x_0, y - y_0)$ in $\mathcal{E}_{BE}$ and using expression (30b) for $\mathcal{E}_s$.

5.4 Linearized form.

Since $\mathcal{E}_s$ is small near the center of the chamber, an approximate expression for the field can be obtained by linearizing $\mathcal{E}_{BE'}$ inside the $1-\sigma$ ellipse, thus

$$\mathcal{E} = \begin{cases} \dfrac{2(\xi - \xi_0)}{\sigma_x + \sigma_y} & \text{for } |\xi - \xi_0| \le 1 \\ \text{Eqs. (29–30)} & \text{for } |\xi - \xi_0| > 1 \end{cases} \tag{39}$$

where the bunch center is assumed to be at location (x_0, y_0), and we have defined $\xi_0 = x_0/\sigma_x + iy_0/\sigma_y$. This "patched" field (39) has the advantage of simplicity over $\mathcal{E}_{BE'}$ but it has the defect of having an unphysical discontinuity[5)] at the $1-\sigma$ ellipse, $|\xi - \xi_0| = 1$.

In previous simulations for the LHC [3] and PEP-II [11] we have used Eq. (39) to compute the beam kick on the electrons. As discussed in Sec. 10.7, we have carried out spot checks that show that Eq. (39) yields estimates for the power deposition on the LHC beam screen that are only $\sim 10\%$ larger than those obtained with Eq. (33).

[4)] The Bassetti-Erskine formula is usually expressed in terms of $\mathcal{E}_y + i\mathcal{E}_x$, which is trivially re-expressed, as we do here, in terms of $\mathcal{E}_x + i\mathcal{E}_y$.

[5)] I am indebted to F. Ruggiero for emphasizing this point.

6 Beam-electron interaction in the impulse approximation.

Let $\mathbf{E}$ and $\mathbf{B}$ be the electric and magnetic fields produced by the bunch, and let $\mathbf{v}_-$ and $-e$ be the velocity and charge of an electron in the cloud. Its equation of motion is, then,

$$\dot{\mathbf{p}} = -e\left(\mathbf{E} + \frac{\mathbf{v}_-}{c} \times \mathbf{B}\right) \simeq -e\mathbf{E} \tag{40}$$

where we have neglected the magnetic force on account of the assumption that the electron is nonrelativistic (just like $\mathbf{E}$, the magnetic field $\mathbf{B}$ is also purely transverse, and its magnitude is comparable to that of $\mathbf{E}$). Thus the momentum change, in the impulse approximation, is obtained by integrating this equation over time t assuming that the electron does not move during the bunch passage,

$$\Delta\mathbf{p} = \int_{-\infty}^{\infty} dt\, \dot{\mathbf{p}} = -\frac{e^2 N_p}{c}\mathbf{F} \tag{41}$$

where we have used the fact that, for a relativistic bunch, the field has the form $\mathbf{E} = \lambda(s-ct)\mathbf{F}(x,y)$, where λ is the longitudinal charge density normalized to the total charge, and $\mathbf{F}$ is a purely transverse vector. In terms of the complex electric field $\mathcal{E}$, Eq. (41) reads

$$\Delta p_x + i\Delta p_y = -\frac{e^2 N_p}{c}\,\mathcal{E} \tag{42}$$

where $e^2/c \simeq 1.44 \times 10^{-9}$ (eV/c)-m.

6.1 Estimate of the largest kick.

From Eq. (32) one finds that the peak value of the electric field from a round gaussian bunch is $\mathcal{E} \simeq z/\sigma^2$ and this value is obtained at $|z| \simeq \sigma$. Therefore the largest kick experienced by an electron is

$$\Delta p \simeq -\frac{e^2 N_p}{c\sigma} \tag{43}$$

Thus, if the electron was initially at rest or moving slowly, and if it remains nonrelativistic after the kick, its energy change is

$$\Delta E = \frac{(\Delta p)^2}{2m} \simeq \frac{1}{2}mc^2\left(\frac{N_p r_e}{\sigma}\right)^2 \tag{44}$$

where $r_e = e^2/mc^2 \simeq 2.818 \times 10^{-15}$ m is the classical radius of the electron. For LHC parameters we obtain $N_p r_e/\sigma = 1$, and hence, in the impulse approximation, the electrons close to the bunch can become relativistic in a single kick. As discussed in more detail below, however, the impulse approximation is not reliable for these electrons, and the energy kick is much smaller owing to bunch length effects [8].

For elliptical gaussian charges, the peak value of the electric field is $\mathcal{E}_{BE} \simeq 2\xi/(\sigma_x + \sigma_y)$ and it obtains near the $1-\sigma$ ellipse, $|\xi| \simeq 1$. Formulas (43) and (44) remain valid provided one makes the replacement $\sigma \to (\sigma_x + \sigma_y)/2$

6.2 Estimate of the kicks received by electrons near the chamber wall.

If an electron is close to the wall of the chamber, we can sensibly represent the bunch by a point-like charge, and we can then estimate the field from Eq. (31). We look only at the "corners"of the ellipse $(x, y) = (a, 0)$, where $(\mu, \phi) = (\mu_c, 0)$, and $(x, y) = (0, b)$, where $(\mu, \phi) = (\mu_c, \pi/2)$. The parameter ϵ defined by

$$\epsilon \equiv e^{-2\mu_c} = \frac{a-b}{a+b} \tag{45}$$

has the value $\epsilon = 0.1$ in our elliptical-shape model of the beam screen for the LHC. Therefore we can sensibly keep only the first term in the series in Eq. (31) and we obtain

$$\mathcal{E}_y(x = 0, y = b) \simeq \frac{2}{b} + \frac{8\epsilon}{g}\frac{\sinh \mu_c}{\cosh 2\mu_c} \tag{46a}$$

$$\mathcal{E}_x(x = a, y = 0) \simeq \frac{2}{a} - \frac{8\epsilon}{g}\frac{\cosh \mu_c}{\cosh 2\mu_c} \tag{46b}$$

Here the first term ($2/a$ or $2/b$) is the direct field, and the second is the contribution from the surface charge (notice the sign difference in the two). The corresponding numerical values are

$$\mathcal{E}_y(x = 0, y = b) \simeq 1.11 + 0.18 = 1.29 \quad \text{cm}^{-1} \tag{47a}$$

$$\mathcal{E}_x(x = a, y = 0) \simeq 0.91 - 0.22 = 0.69 \quad \text{cm}^{-1} \tag{47b}$$

so that the surface charges have about a $\pm 20\%$ effect on the field.

In the impulse approximation, the corresponding energy kick received by an electron at rest at either of these two corners is

$$\Delta E(x = 0, y = b) \simeq 380 \quad \text{eV} \tag{48a}$$

$$\Delta E(x = a, y = 0) \simeq 109 \quad \text{eV} \tag{48b}$$

and the corresponding velocity changes are

$$\Delta v_y(x = 0, y = b) \simeq 1.2 \quad \text{cm/ns} \tag{49a}$$

$$\Delta v_x(x = a, y = 0) \simeq 0.63 \quad \text{cm/ns} \tag{49b}$$

Since the bunch spacing is $\simeq 25$ ns, these numbers imply that, in the absence of a magnetic field, an electron at the wall that is kicked by a bunch will reach the opposite side of the chamber long before the next bunch comes by. For a strong vertical magnetic field, this conclusion is true only for the vertical motion.

One might think that this would imply that all electrons created by the photoelectric process reach the opposite wall almost instantly upon the passage of a bunch. This is not quite true for two reasons: (a) most electrons receive a weaker kick on account of the time-of-creation modulating factor (9), and (b): bunch length effects can substantially reduce the energy transfer from the bunch to an electron due to transverse oscillations of the electron near the bunch during the bunch passage [8].

7 Bunch length effects.

7.1 Criterion for the validity of the impulse approximation.

The impulse approximation used in Eq. (41) is valid provided that the forces act on a time scale so short that the electron remains essentially at rest during this time. A

practical criterion for the validity of this approximation in the absence of a magnetic field can be found as follows: Consider an electron at rest, or moving sufficiently slowly, at a distance r from the beam, where $r \gg \sigma_x, \sigma_y$. Neglecting surface charges, the momentum kick is given by Eq. (41), namely

$$\Delta p \simeq -\frac{e^2 N_p}{c}\,\frac{2}{r} \tag{50}$$

For a weak enough kick the electron remains nonrelativistic, and the corresponding velocity change is $\Delta v = \Delta p/m$. The characteristic length of time during which the field acts on the electron is σ_t, the rms bunch length in units of time. During this time the electron moves a distance $\Delta r = \Delta v \sigma_t$. Then the criterion for the validity of the impulse approximation is $\Delta r \ll r$, or

$$\frac{2e^2 N_p \sigma_t}{mcr} \ll r \tag{51}$$

Using $\sigma_t = \sigma_z/c$ the criterion is written

$$2N_p \frac{r_e \sigma_z}{r^2} \ll 1 \tag{52}$$

This criterion can be turned around to define a radius r_i that roughly defines the transverse region of validity of the impulse approximation. For this we choose 0.1 to be a practical measure of smallness in Eq. (52) so that

$$r_i = \sqrt{20 N_p r_e \sigma_z} \tag{53}$$

The impulse approximation is approximately valid for electrons that are at distances from the bunch larger than r_i at the time the bunch passes. For nominal LHC parameters, we obtain $r_i = 2$ cm, which is comparable to the radius of the beam screen. Therefore, the impulse approximation is not valid for any electrons, except perhaps those that are very close to the beam screen.

7.2 Slicing the bunch.

As in beam-beam simulations, bunch length effects are taken into account by a "thick-lens" element, which is implemented by a succession of a certain number N_k of weighted thin-lens (impulse) kicks separated by free-particle drifts (in the presence of a dipole magnetic field the free-particle drift is replaced by the appropriate helical motion).

We assume that the longitudinal charge distribution of the bunch is described by a density $\hat{\lambda}(z)$ where the caret is meant to emphasize unit normalization. For the purposes of our simulations, we replace this density by a weighted superposition of N_k delta functions,

$$\hat{\lambda}(z) \to \hat{\lambda}_s(z) \equiv \sum_{k=-\ell}^{\ell} w_k \delta(z - z_k) \tag{54}$$

where $N_k \equiv 2\ell + 1$ (we assume, for simplicity, that N_k is an odd integer). Each delta function gives rise to a kick at a location z_k weighted by w_k; these locations and weights must be determined according to a certain algorithm. The symmetry $\hat{\lambda}(-z) = \hat{\lambda}(z)$ implies that the kick locations and weights must obey the basic constraints

$$z_{-k} = -z_k \quad \text{and} \quad w_{-k} = w_k \tag{55}$$

In addition, we require that the accumulated effects of the kicks should be the same as in the original distribution, *i.e.*, $\int dz\hat{\lambda}(z) = \int dz\hat{\lambda}_s(z) = 1$, which implies

$$\sum_{k=-\ell}^{\ell} w_k = 1 \tag{56}$$

For the impulse approximation, $N_k = 1$, there is a single kick at the center of the bunch, namely

$$z_0 = 0, \qquad w_0 = 1 \qquad (N_k = 1), \tag{57}$$

but for $N_k > 1$ there is, of course, an infinite number of possible algorithms to decide the w_k's and z_k's consistent with Eqs. (55).

In an ideal calculation one would use an infinite number of kicks. In practice, of course, one wants to use as few as possible for a given desired computational accuracy. Each algorithm has advantages and drawbacks regarding computational efficiency and convergence rate as $N_k \to \infty$. All results presented in this note were obtained with the "equal-spacing" algorithm, described below. We have verified that the "equal-weight" algorithm [22] yields qualitatively similar results. The equal-spacing algorithm, however, is advantageous in the case of a dipole magnetic field because, owing to the even spacing, the computer code section for the drifts between kicks is simpler and faster than in the equal-weight algorithm.

In the equal-spacing algorithm the kicks are chosen to be equally spaced and the weights are proportional to the density at z_k, namely

$$\left.\begin{aligned} z_k &= k\Delta z \\ w_k &= \frac{\hat{\lambda}(z_k)}{\sum\limits_{m=-\ell}^{\ell} \hat{\lambda}(z_m)} \end{aligned}\right\} \qquad k = 0,\ \pm 1, \cdots,\ \pm\ell \qquad (N_k \geq 3) \tag{58}$$

where Δz is the spacing. In our simulations we have considered only a longitudinal gaussian distribution, $\hat{\lambda}(z) = e^{-z^2/2\sigma_z^2}/\sqrt{2\pi}\sigma_z$, and we have chosen, after some experimentation,

$$\Delta z = \frac{3\sigma_z}{N_k - 1} \tag{59}$$

corresponding to a distance $3\sigma_z$ between the first and last kicks. This is our algorithm of choice for the LHC applications.

Results for the convergence rate as a function of the number of kicks for a dipole bending magnet and for a field-free region are shown in Sec. 10.2. We can see that a gaussian bunch is well approximated by 51 kicks evenly-spaced by Δz as specified by Eq. (59).

7.3 The long-bunch mapping.

In the simulation code POSINST each electron is represented by its six-dimensional phase space coordinates plus a time variable. This latter represents how much time there is left till the next bunch comes by. Successive physical operations, such as beam kick, drift, space-charge force, and utilities such as binning and averaging, act on the phase space at specific times and "debit" the time variable, if appropriate. Thus the basic unit of time in the code is the bunch interval s_B/c. This is a well-defined concept in the

impulse approximation in which the bunches have effectively zero length. When bunch length effects are taken into account, however, there is no longer a sharply defined time step, even though s_B/c is still the center-to-center bunch interval.

A convenient way to recover the basic time step s_B/c (and thus the basic structure of the code) is to represent the action of the bunch by an instantaneous mapping which changes both the coordinates and the momenta of the electron. This can be implemented easily if one neglects the action of the space-charge forces during the passage of a given bunch, which is a reasonable approximation for the LHC.

For the sake of illustration, consider the case of a bunch divided up into 2ℓ slices according to the equal-spacing algorithm, *i.e.*, there are $N_k = 2\ell+1$ kicks evenly-spaced by a time step $\Delta t = 3\sigma_z/2\ell c$. Let $\mathbf{X}(t)$ be the 6-dimensional phase space of a given electron at time t and let t_0 be the instant of passage of the center of the bunch. Then the action of the bunch is represented by

$$\begin{aligned}&\mathbf{X}(t_0+\ell\Delta t) = \\ &\quad K(t_0+\ell\Delta t)D(\Delta t)K(t_0+(\ell-1)\Delta t)D(\Delta t)\cdots D(\Delta t)K(t_0-\ell\Delta t)\mathbf{X}(t_0-\ell\Delta t)\end{aligned} \tag{60}$$

where $K(t+k\Delta t)$ represents the action of kick k weighted by w_k,

$$K(t+k\Delta t): \quad p_x + ip_y \to p_x + ip_y - \frac{e^2 N_p}{c}\, w_k\, \mathcal{E} \tag{61}$$

and $D(\Delta t)$ represents the drift between successive kicks.[6)] By multiplying Eq. (60) from the left by $D(-\ell\Delta t)$ and inserting $1 = D(-\ell\Delta t)D(\ell\Delta t)$ just in front of $\mathbf{X}(t_0-\ell\Delta t)$ one can write

$$\mathbf{X}_f(t_0) = \mathcal{K}(t_0)\mathbf{X}_i(t_0) \tag{62}$$

where

$$\begin{aligned}\mathcal{K}(t_0) &= D(-\ell\Delta t)K(t_0+\ell\Delta t)D(\Delta t) \\ &\quad \times K(t_0+(\ell-1)\Delta t)D(\Delta t)\cdots D(\Delta t)K(t_0-\ell\Delta t)D(-\ell\Delta t)\end{aligned} \tag{63}$$

represents the long-bunch mapping. The initial and final phase space vectors $\mathbf{X}_i(t_0)$ and $\mathbf{X}_f(t_0)$ are the pure-drift-transforms of the physical initial and final phase space vectors $\mathbf{X}(t_0-\ell\Delta t)$ and $\mathbf{X}(t_0+\ell\Delta t)$, respectively. It is important to note that the only physical elements that are allowed to act on the electron between $t_0-\ell\Delta t$ and $t_0+\ell\Delta t$ are drifts and kicks. In particular, if the electron hits the wall of the chamber during this interval one cannot use this map without some modification.

8 Simulation procedure.

Our computer program POSINST simulates the dynamics of the electron cloud following the same general procedure as in Ref. 23. The code simulates the cloud within one single specified section of the ring.

One of the basic inputs to the simulation is the average number of photoelectrons per bunch passage, $\bar{N}_e$, given by Eq. (5). In the simulation we represent the $\bar{N}_e$ photoelectrons by a *fixed number* of macro-particles, $N_{\rm phel}$, which are generated at every bunch passage at the walls of the section. For $R \lesssim 1$, these are distributed in position, angle and energy

[6)] In a field-free region $D(\Delta t)$ represents straight-line motion during a time Δt; in a dipole magnet, $D(\Delta t)$ represents helical motion during a time interval Δt.

as described in Sec. 3. These electrons are then kicked by successive bunches as they traverse the section. The motion of the electrons is fully 3-dimensional. In between kicks, the motion of any given electron is computed exactly (a straight line at constant velocity in a field-free section, or a helical motion in a dipole field), and from this trajectory we obtain the instant and the location of the collision point of the electron with the wall. At this point, the electron is either absorbed or creates secondary electrons according to the SEY model described in Sec. 4. Space-charge effects are included in the motion of the electrons in the cloud, as explained in Sec. 8.2.

The code can also compute the effective dipole wake function due to the electron cloud and from it the coupled-bunch instability growth rate [2, 3]. In this note, however, we only focus on the heat deposition from the electrons on the beam screen and related quantities.

8.1 Macroparticle-to-particle factor.

In practice, one cannot simulate the electron cloud with a realistic number of particles, which is expected to be in the range $10^8 - 10^{10}$ per section, since this number is too large for present-day computers. Thus one resorts to simulating a much smaller number of representative particles, usually referred to as "macroparticles." In order to obtain quantitative results from the simulation that can be compared with a real machine, one must scale all electron-density-dependent quantities obtained from the simulation by a density factor $\mathcal{F}$, which can also be interpreted as the macroparticle-to-particle charge ratio, given by

$$\mathcal{F} = \frac{\text{number of electrons in reality}}{\text{number of electrons in the simulation}} \tag{64}$$

Both the numerator and denominator in Eq. (64) are a priori unknown, so we need a more convenient expression for $\mathcal{F}$. Since the basic input value to our simulation is the number of macro-photoelectrons per bunch passage, N_{phel}, we can express $\mathcal{F}$ as

$$\mathcal{F} = \frac{\bar{N}_e}{N_{\text{phel}}} \tag{65}$$

The numerator in this formula is the total number of real photoelectrons created in the section being simulated during a time interval equal to a bunch spacing, s_B/c, while the denominator is the corresponding number of macro-photoelectrons, each carrying a charge $e\mathcal{F}$. Eqs. (65) and (64) are equivalent because the number of electrons in existence in the simulation (and in reality) is directly proportional to the number of photoelectrons.

8.2 Space-charge forces.

In order to compute the space-charge forces from the electrons on themselves, we make the simplifying assumption that the electron density is, on average, longitudinally uniform so that the field calculation becomes effectively two-dimensional. Let's say we are simulating one section of length L, *i.e.*, one dipole magnet of length L, or one field-free section of length L. The equation to solve is

$$\nabla \cdot \mathbf{E} = 4\pi\rho_e \tag{66}$$

where $\mathbf{E}$ is the space-charge electric field and ρ_e is the electron charge density,

$$\rho_e(x, y, s) = -e \sum_j \delta^{(2)}(\mathbf{x} - \mathbf{x}_j)\delta(s - s_j) \tag{67}$$

where $(x, y, s) \equiv (\mathbf{x}, s)$ is the observation point, and $(\mathbf{x}_j, s_j)$ is the location of the j-th electron ($\mathbf{x}$ and $\mathbf{x}_j$ represent here the two-component transverse vectors). Owing to the assumption of longitudinal uniformity of ρ_e, the average electric field must be of the form

$$\mathbf{E} = (E_x(x, y), E_y(x, y), 0) \tag{68}$$

so that, integrating Eq. (66) over the longitudinal coordinate s over the entire section length L yields the two-dimensional equation

$$\nabla_\perp \cdot \mathbf{E}_\perp = -\frac{e}{L} \sum_j \delta^{(2)}(\mathbf{x} - \mathbf{x}_j) \tag{69}$$

where $\mathbf{E}_\perp \equiv (E_x, E_y)$. It follows from the discussion in Sec. 5 that the solution of this equation, subject to the elliptical perfect-conductor boundary, is given in complex form by the superposition

$$E_x + iE_y = -\frac{e}{L} \sum_j (\mathcal{E}_d + \mathcal{E}_s)_j \tag{70}$$

where $\mathcal{E}_d$ and $\mathcal{E}_s$ are given by Eqs. (30a) and (30b) with the replacement $z_0 \to z_j = x_j + iy_j$.

The momentum kick received by a given electron during a time interval Δt that is short on the time scale of macroscopic changes in ρ_e is obtained by integrating the equation $\dot{\mathbf{p}} = -e\mathbf{E}$, yielding

$$\Delta p_x + i\Delta p_y = G \sum_j (\mathcal{E}_d + \mathcal{E}_s)_j \tag{71}$$

where the space-charge kick factor is $G = e^2 \Delta t / L$. In our simulations we divide the time interval between bunches, s_B/c, into an integral number K_s of steps (typically $K_s = 4 - 16$), and apply the space-charge kick (71) at each step. Thus $\Delta t = s_B/cK_s$, and

$$G = \frac{e^2}{c} \frac{\mathcal{F} s_B}{L K_s} \tag{72}$$

where we have included the superparticle charge factor $\mathcal{F}$, Eq. (65), in order to account for the fact that we are simulating macroparticles rather than true electrons.

Eq. (71) represents an "N^2 algorithm" for the space-charge kick, since $\Delta p_x + i\Delta p_y$ has to be computed for all the electrons in the cloud. Since this computation can be prohibitively CPU-intensive, we have resorted to a grid method to speed it up at the expense of some accuracy. For this we define a rectangular grid in (x, y) space with cell size $\Delta x \times \Delta y$. We first compute the transverse electric field $\mathcal{E}$ at all the grid points k by simply superposing the fields from all the electrons,

$$\mathcal{E}_k = \sum_j (\mathcal{E}_d + \mathcal{E}_s)_j \tag{73}$$

and then we compute the kick $\Delta p_x + i\Delta p_y$ on each electron by an area-weighted average of the fields at the four grid points nearest the electron [24]. Typically we use a grid cell $\Delta x \times \Delta y = 5 \times 5$ mm, with spot checks down to 1×1 mm. We typically make the approximation of computing the grid fields only once per bunch interval, immediately after the bunch passage, and then we apply the space-charge kick K_s times. We have carried out spot-checks in which we compute the space-charge fields K_s times per bunch interval s_B/c, *i.e.*, at every step, as discussed in Sec. 10.8.

9 Results.

Table 2 collects most of the parameter values used in our simulations, already mentioned in the text. The column labeled "reference case" represents what we believe are sensible parameter values whose purpose is to provide a point of departure for comparisons. Some of these parameters correspond to initial measurements of surface properties of the beam screen at the EPA [26].

Table 2: Parameter values and simulation conditions.

	range of values explored	reference case
Beam		
Particles per bunch, N_p	1.05×10^{11}	1.05×10^{11}
Bunch spacing, s_B [m]	7.48	7.48
RMS transverse beam size, σ [mm] (shape)	0.3 (round gaussian)	0.3 (round gaussian)
RMS bunch length, σ_z [cm] (shape)	7.7 (gaussian)	7.7 (gaussian)
Photoemission		
Photon reflectivity, R	~ 1	~ 1
Quantum efficiency, Y'	0.02–1	0.2
Photons per proton, $N_{\gamma/p}(E_\gamma \geq 4$ eV)	0.18	0.18
Peak energy of distribution, E_{ph} [eV]	5 or 10	5
Energy width of distribution, σ_{ph} [eV]	5 or 10	5
Angular distribution	$\cos\theta$, uncorrelated	$\cos\theta$, uncorrelated
Secondary emission		
Peak SEY at normal incidence, $\hat{\delta}(0)$	0–1.8	1.3
Electron energy at SEY peak, $\hat{E}(0)$ [eV]	400	400
Angular dependence of SEY	Eqs. (17)	Eqs. (17)
Emitted electron parameter p	2	2
Emitted electron energy width parameter, E_s [eV]	5 or 10	5
Angular distribution of emitted electrons	$\cos\theta$, uncorrelated	$\cos\theta$, uncorrelated
Elastic and rediffused components included?	yes or no	no
Simulation method		
Macro-photoelectrons per bunch, N_{phel}	100	100
Steps per bunch interval, K_s	$1 - 16$	4
Space-charge grid, $\Delta x \times \Delta y$ [mm]	$1 \times 1 - 5 \times 5$	5×5
Space-charge computation frequency during s_B/c	$1 - K_s$ times	1 time
Kicks per bunch, N_k	$1 - 101$	51
Distance between outermost kicks	$3\sigma_z$	$3\sigma_z$

9.1 Power deposition in the arc dipole magnets.

Figure 5 shows the power deposition per unit length in the dipole bending magnets as a function of Y' for 4 values of $\hat{\delta}$. One can see that when $\hat{\delta}$ exceeds a certain threshold, the power deposition has a nonvanishing limit when $Y' \to 0$. This implies that, if the SEY is high enough, there is substantial power deposition due to a self-sustaining beam-induced multipacting effect [25]. In this case, the phenomenon may start from just one seed electron which may originate from ionization of the residual gas.

9.2 Dependence on $\hat{\delta}$.

Figure 6 shows the power deposition per unit length in the dipole bending magnets as a function of $\hat{\delta}$ for $Y' = 0.2$. There is a clear threshold at $\hat{\delta} \simeq 1.4$ beyond which there is a qualitative increase in the power deposition, as discussed in the previous section.

The notion of a critical value for $\hat{\delta}$ has been discussed in Ref. 9 and studied more systematically in Ref. 10. The concept can be extended by noting that the ECE exhibits phases that are qualitatively analogous to those of a ferromagnet with the correspondence given in Table 3. It is possible that the phase structure of the ECE is more complicated than that of a simple ferromagnet; we shall map out the phase diagram in parameter space in a separate note.

Table 3: Ferromagnet analog of the ECE.

Electron Cloud		Ferromagnet
peak value of SEY, $\hat{\delta}$	$\longleftrightarrow$	inverse temperature, β
quantum efficiency, Y'	$\longleftrightarrow$	applied magnetic field, H
power deposition	$\longleftrightarrow$	magnetization, M

9.3 Power deposition in the field-free regions in the arcs.

Figure 7 shows the power deposition calculated in the field-free regions in the arcs. Comparing with Fig. 5, one sees that the power deposition is 2–6 times larger than in the dipole magnets.

10 Discussion and conclusions.

10.1 General comments.

Our result for the reference case show a power deposition of ~ 0.75 W/m for the dipole bending magnets and ~ 4.1 W/m for the field-free regions in the arcs. The power deposition scales roughly linearly with the quantum efficiency Y' provided the peak value of the SEY, $\hat{\delta}$, is below a critical value ~ 1.4. If $\hat{\delta}$ exceeds this critical value there is substantial power deposition due to a self-sustaining beam-induced multipacting condition. As evidenced by the results presented in the following sections, there is a strong sensitivity to the characteristic energy E_s of the emitted secondary electrons in the range $E_s = 5 - 10$ eV.

Our results are in good agreement with those in Ref. 10 for those cases in which a direct comparison is possible. Relatively small numerical discrepancies can be attributed to differences in the detailed approximations and physical models used by the codes. For example, one such difference is in the energy distribution of the secondary electrons: while we assume $d\delta/dE \propto E \exp(-E/E_s)$, the model used in Ref. 10 is of the form $d\delta/dE \propto \exp(-(E/E_s)^2)$. These two models are probably equivalent on the level of precision with which these distributions are known on the scale of a few eV, and therefore the spread in the results from the two codes must be regarded as representative of the uncertainties at this stage of the calculation.

This agreement strengthens our confidence in the methods used to simulate the ECE, and re-emphasizes the relevance of low-energy secondary emission parameters for the power deposition in the LHC beam screen. Since these parameters are used as input

to our computer program, it is vital to pin them down in order to obtain a more reliable estimate of the power deposition from our simulations.

In order to test the sensitivity of our calculation to different physical parameters and simulation conditions, we shall now present the estimates obtained for the power deposition by changing one or a few parameters at a time away from the reference case.

10.2 Convergence as a function of the number of kicks.

Fig. 8 shows the calculated power deposition by the electrons as they hit the walls of the chamber. Except for N_k, all parameters correspond to the reference case. It can be seen that adequate convergence is achieved for $N_k = 51$. All other results presented in this note assume this value for N_k.

10.3 Dependence on E_{ph} and σ_{ph}.

If the photoemission parameters E_{ph} and σ_{ph} are both set to 10 eV instead of 5 eV while all others are kept fixed at their reference values, the power deposition in the dipole magnets increases from $\sim$ 0.75 W/m to $\sim$ 0.86 W/m. This relatively mild sensitivity is presumably due to bunch length effects, particularly the time-of-creation modulating factor (9).

10.4 Dependence on E_s.

An important parameter is the energy an electron needs in order to cross the chamber in one bunch spacing. If an electron is created at rest at $x = 0, y = b$, it needs a speed $v_y = 2bc/s_B$ in order to cross the chamber, and the corresponding energy is

$$E_{\min} = 2mc^2 \left(\frac{b}{s_B}\right)^2 = 6 \text{ eV} \tag{74}$$

If an electron is created at the surface of the screen with an energy lower than this, it may be strongly kicked by the next bunch that comes by, resulting in a substantial collision energy at the walls. Of course, in our model the electrons are created with a continuous energy-angle distribution, so there is no sharp energy boundary that separates the slow electrons from the fast. Nevertheless, the energy scale ~ 6 eV is important [12]. To test the sensitivity of the power deposition to low-energy secondary electrons we have run a simulation in which the energy scale parameter E_s is increased from 5 to 10 eV. The results for the dipole bending magnets is shown in Fig. 9. One can see that the power deposition is down by roughly 50% with respect to the case in which $E_s = 5$ eV, shown in Fig. 5. One can also see that there is no self-sustaining beam-induced multipacting effect up to $\hat{\delta} = 1.8$. Presumably, such an effect occurs at larger values of $\hat{\delta}$.

10.5 Backscattered and rediffused electrons.

If the elastically backscattered and rediffused components of the SEY are included, the spectrum $d\delta/dE$ acquires a high-energy peak at $E \lesssim E_0$ from the former, and a fairly constant, but small, contribution in the whole range $0 \lesssim E < E_0$ from the latter [11], as seen in Fig. 10. Perhaps more importantly, these components add an excess of secondary electrons for $E_0 \lesssim 5$ eV, as shown in Fig. 11. These extra low-energy electrons have an effect on the power deposition similar to that discussed in Sec. 10.4. A spot-check for the dipole magnets for the reference case shows that the power deposition increases from $\sim$ 0.75 W/m to $\sim$ 1.9 W/m when the elastic and rediffused components of the SEY are included.

10.6 Dependence on K_s.

A spot-check indicates that the number of steps K_s between bunches does not have a dramatic effect on our estimates. For the reference case the estimate of the power deposition in the dipole magnets increases from ~ 0.75 W/m to ~ 0.87 W/m when K_s is increased from 4 to 16. A similar calculation for the field-free sections shows that the power deposition increases from ~ 4.1 W/m to ~ 4.2 W/m.

10.7 Linearized *vs.* smooth E-field.

As mentioned in Sec. 5.4, our preliminary estimates [3] were obtained with a linearized form of the electric field given by Eq. (39). A spot-check indicates that this approximation does not have a dramatic effect: for the reference case the estimate of the power deposition in the dipole magnets increases from ~ 0.75 W/m, obtained with the smooth field (33), to ~ 0.85 W/m obtained with the linearized field (39). This result implies that this approximation, by itself, did not entail a significant error in our preliminary estimates.

For an elliptical gaussian bunch the linearized form (39) represents a significant savings of computer time over the modified Bassetti-Erskine formula (37). For a round gaussian bunch, however, the time savings is marginal. For this reason, we have not used (39) in all other results presented in this note.

10.8 Space-charge field computed at every step.

In all simulation results discussed above we have simplified the calculation by computing the space-charge fields only once per bunch interval, immediately following the passage of a bunch, and then applying the kick from these fields K_s times before the next bunch comes by. The purpose of this approximation, of course, is to save computer time. A more physical description requires the recomputation of the space-charge fields K_s times, *i.e.*, once per time step. A spot check for $K_s = 4$ indicates that the short-cut approximation does not have a dramatic effect on our estimates: for the reference case, the estimate of the power deposition in the dipole magnets increases from ~ 0.75 W/m, obtained with the short-cut approximation, to ~ 0.82 W/m obtained from a recomputation of the space-charge fields K_s times. For higher values of Y' and/or $\hat{\delta}$, however, there is a larger difference between the two approximations owing to the higher electron-cloud density [10].

10.9 Finer space-charge grid.

In all results presented above the space-charge grid size was set to 5×5 mm. If we set it to 1×1 mm and we use $K_s = 16$ steps with the space-charge fields computed at every step, the results also do not show a dramatic change. For the reference case the estimate of the power deposition in the dipole magnets increases from ~ 0.75 W/m to ~ 0.83 W/m.

11 Acknowledgments.

I am indebted to G. Lambertson for continued collaboration. I am most grateful to O. Brüning for extensive discussions and comparisons of our results, and to O. Gröbner and I. Collins for sharing measured data on the beam screen before publication. I am also grateful to J. Bisognano, R. Calder, C. Fadley, W. Fawley, E. Gullikson, S. Heifets, N. Hilleret, D. Hunt, K. Kennedy, K.-J. Kim, K. Ohmi, J. Peterson, R. Rimmer, J. Rogers, F. Ruggiero, T. Stevens, W. Stoeffl, W. Turner, K. Yokoya, A. Zholents, F. Zimmermann,

M. Zisman and M. Zolotorev for many discussions over time. I am grateful to F. Schmidt for help in typesetting and to NERSC for supercomputer support.

References

[1] O. Gröbner, "Technological Problems Related to the Cold Vacuum System of the LHC," Vacuum **47**, pp. 591–595 (1996).

[2] F. Zimmermann, "A Simulation Study of Electron-Cloud Instability and Beam-Induced Multipacting in the LHC," LHC Project Report 95, 27 February 1997.

[3] M. A. Furman, "Comments on the The Electron-Cloud Effect in the LHC Dipole Bending Magnets," KEK Proceedings 97-17, p. 234, December 1997 (Proc. MBI-97 workshop, KEK, Tsukuba, Japan, 15–18 July 1997; Y. H. Chin, ed.)

[4] F. Zimmermann, "Electron-cloud instability and beam-induced multipacting in the LHC and in the VLHC," KEK Proceedings 97-17, p. 221, December 1997 (Proc. MBI-97 workshop, KEK, Tsukuba, Japan, 15–18 July 1997; Y. H. Chin, ed.).

[5] O. Gröbner, "Bunch-Induced Multipacting," to be published in the Proc. PAC97, Vancouver, BC, May 12–16, 1997.

[6] O. S. Brüning, "Simulations for the beam-induced electron cloud in the LHC liner," LHC project note 102, August 1997.

[7] J. B. Jeanneret, "Photoemission in LHC-a simple model," CERN SL/Note 97-48 (AP), 14 June 1997.

[8] J. S. Berg, "Energy Gain in an Electron Cloud During the Passage of a Bunch," LHC project note 97, 1 July 1997.

[9] G. V. Stupakov, "Photoelectrons and Multipacting in the LHC: Electron Cloud Build-Up," LHC Project Report 141, October 1997.

[10] O. S. Brüning, "Simulations for the beam-induced electron cloud in the LHC beam screen with magnetic field and image charges," LHC Project Report 158, 7 November 1997.

[11] M. A. Furman and G. R. Lambertson, "The Electron Cloud Effect in the arcs of the PEP-II Positron Ring," KEK Proceedings 97-17, p. 170, December 1997 (Proc. MBI-97 workshop, KEK, Tsukuba, Japan, 15–18 July 1997; Y. H. Chin, ed.).

[12] F. Ruggiero, LHC seminar, 30 October, 1997.

[13] "The Large Hadron Collider: Conceptual Design," CERN/AC/95-05(LHC), 20 October 1995.

[14] P. M. Morse and H. Feschbach, *Methods of Theoretical Physics*, McGraw-Hill, 1953, ch. 10.

[15] H. Bruining, *Physics and Applications of Secondary Electron Emission*, Pergamon Press, 1954.

[16] H. Seiler, "Secondary Electron Emission in the Scanning Electron Microscope," J. Appl. Phys. **54**(11), Nov. 1983, pp. R1–R18.

[17] R. Kirby and F. King, private communications, Dec. 1996–Feb. 1997.

[18] P. A. Redhead, J. P. Hobson and E. V. Kornelsen, *The Physical Basis of Ultrahigh Vacuum*, Chapman and Hall, Ltd., 1968, ch. 4 (reprinted by the AIP in 1993 as part of the American Vacuum Society Classics series).

[19] M. v. Ardenne, *Tabellen der Elektronenphysik, Ionenphysik und Übermikroskopie*, vol. 1, Veb Deutscher Verlag der Wissenschaften, 1956.

[20] *Handbook of Mathematical Functions*, M. Abramowitz and I. A. Stegun, Eds., Dover Publications Inc., 9th printing, 1970.

[21] M. Bassetti and G. A. Erskine, "Closed Expression for the Electric Field of a Two-Dimensional Gaussian Charge," CERN-ISR-TH/80-06.
[22] M. A. Furman, A. Zholents, T. Chen and D. Shatilov, "Comparisons of Beam-Beam Simulations," LBL-37680/CBP Tech Note-152/PEP-II AP Note 95.39, Proc. Seventh Advanced ICFA Workshop on Beam Dynamics, JINR, Dubna, Russia, 18-20 May, 1995, pp. 123–142.
[23] K. Ohmi, "Beam Photo-Electron Interactions in Positron Storage Rings," Phys. Rev. Lett. **75**(8), pp. 1526–1529 (1995).
[24] R. W. Hockney and J. W. Eastwood, *Computer Simulation Using Particles*, Inst. of Physics Publishing, 1988.
[25] O. Gröbner, "Bunch-Induced Multipactoring," Proc. 10th Intl. Accel. Conf., Serpukhov, 1977, pp. 277–282.
[26] I. Collins, private communication, Aug. 1997.

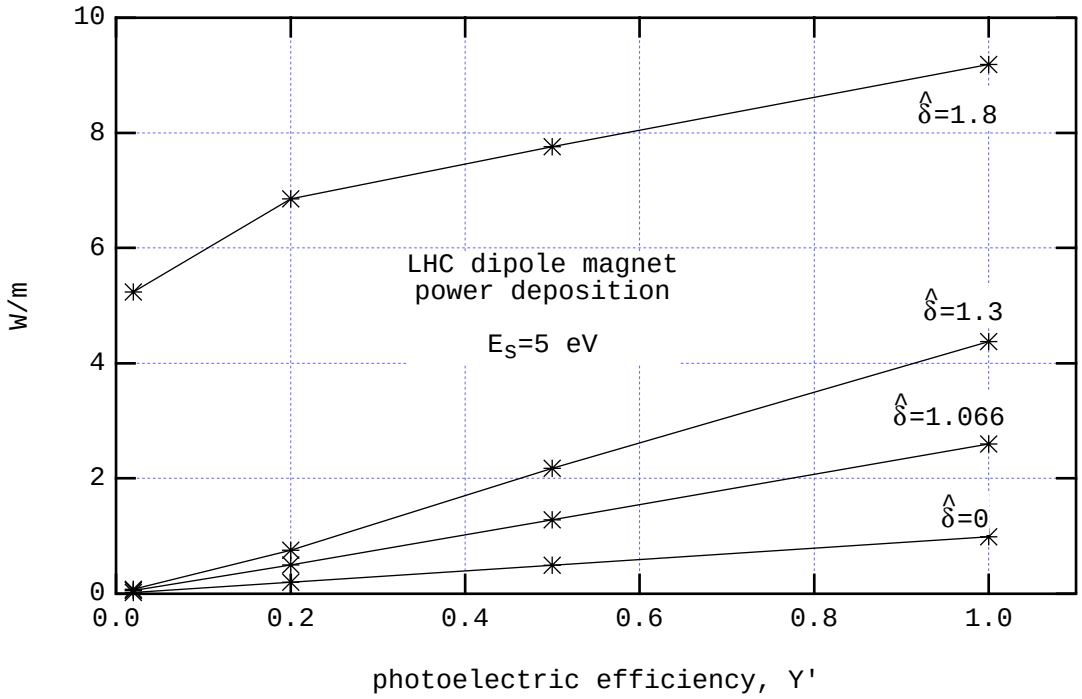

Figure 5: Power deposition per unit length in the dipole bending magnets. All parameters correspond to the reference case except for Y' and $\hat{\delta}$, whose values are labeled.

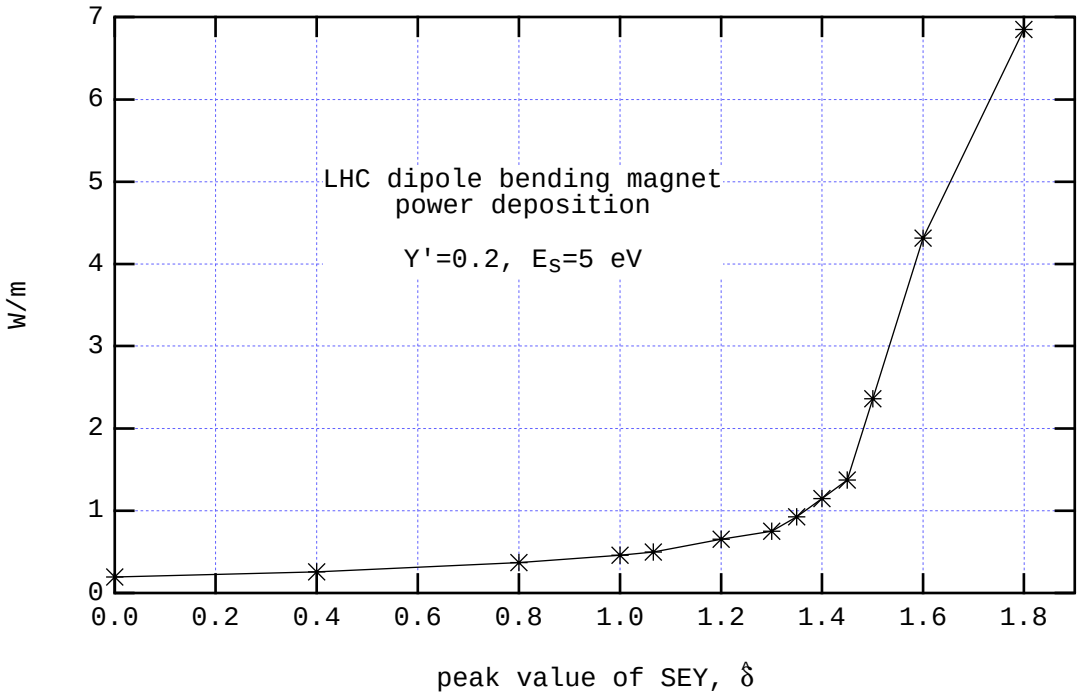

Figure 6: Power deposition per unit length in the dipole bending magnets as a function of $\hat{\delta}$ for fixed $Y' = 0.2$. All other parameters correspond to the reference case.

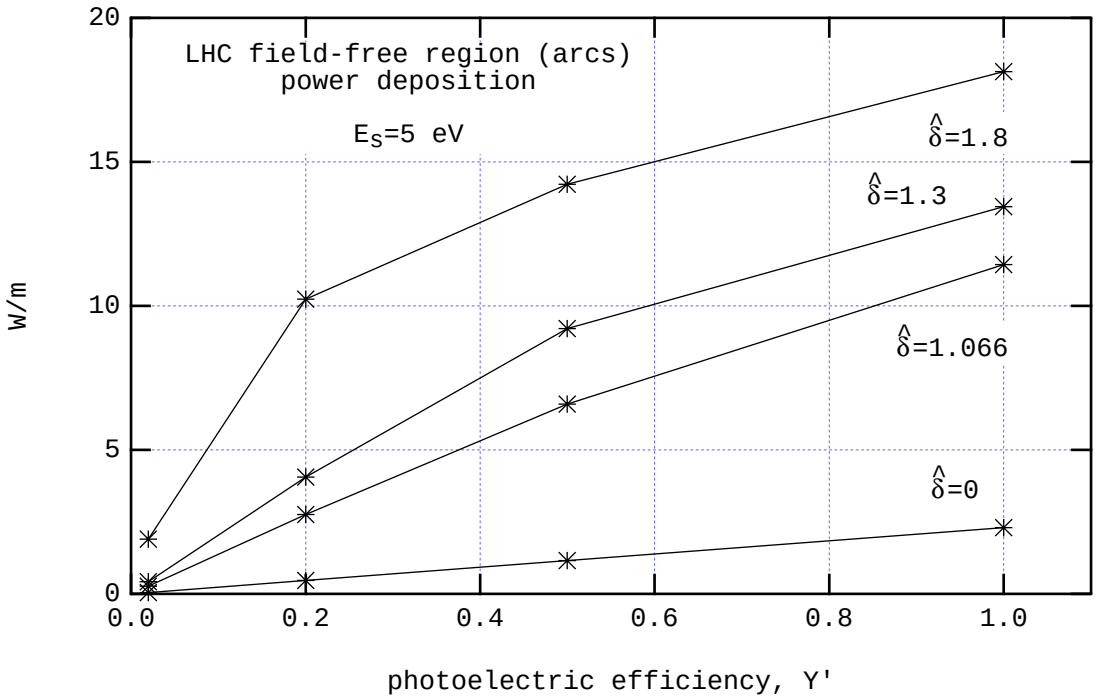

Figure 7: Power deposition per unit length in the field-free regions in the arcs. All parameters correspond to the reference case except for Y' and $\hat{\delta}$, whose values are labeled.

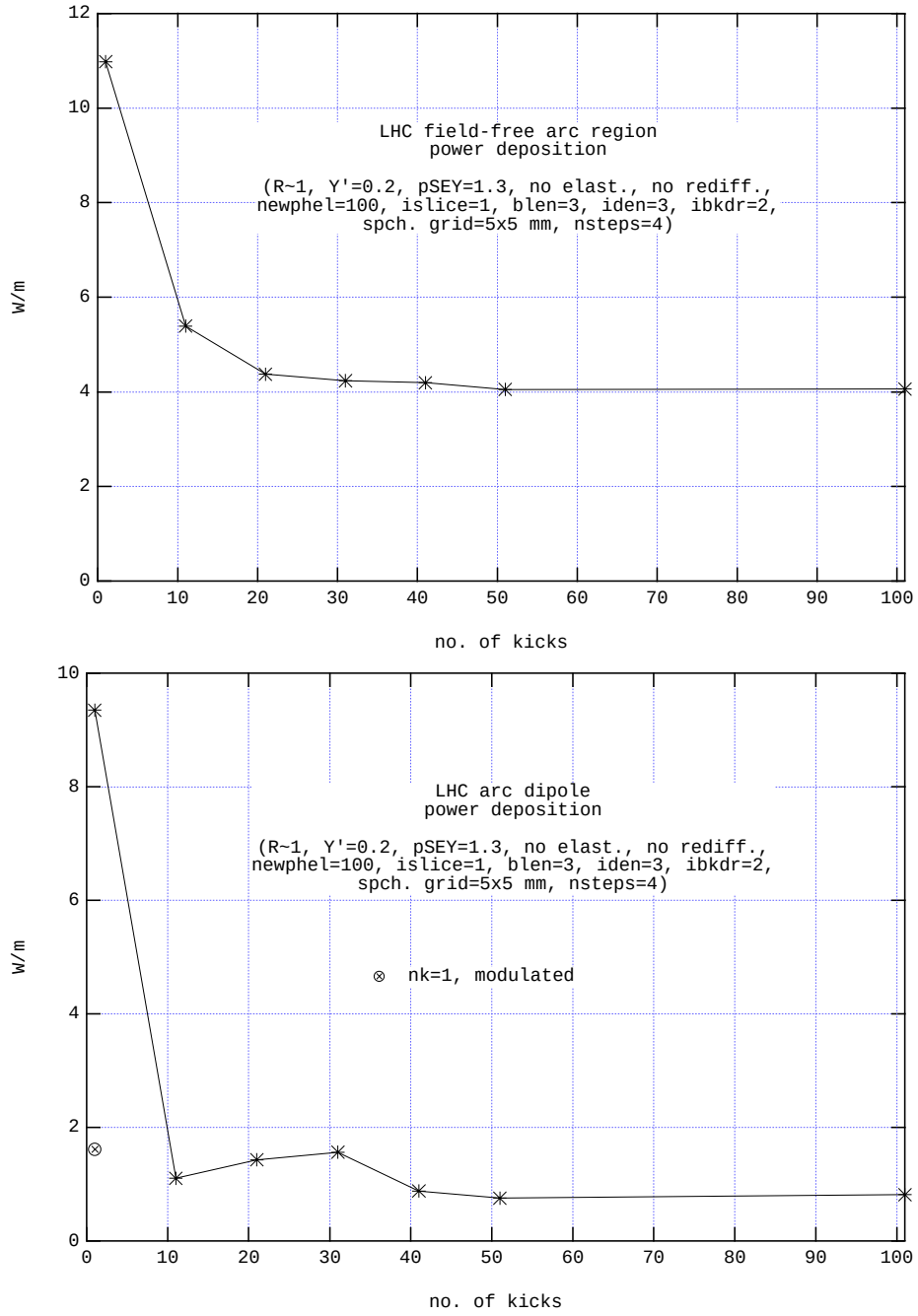

Figure 8: Convergence rate of the power deposition as a function of the number of kicks. Top: field-free section. Bottom: dipole bending magnet. In this latter case, the isolated point on the graph for 1 kick, labeled "nk=1, modulated," represents the result of using the impulse approximation modified by a cyclotron phase factor, as described in Sec. 6 of Ref. 3.

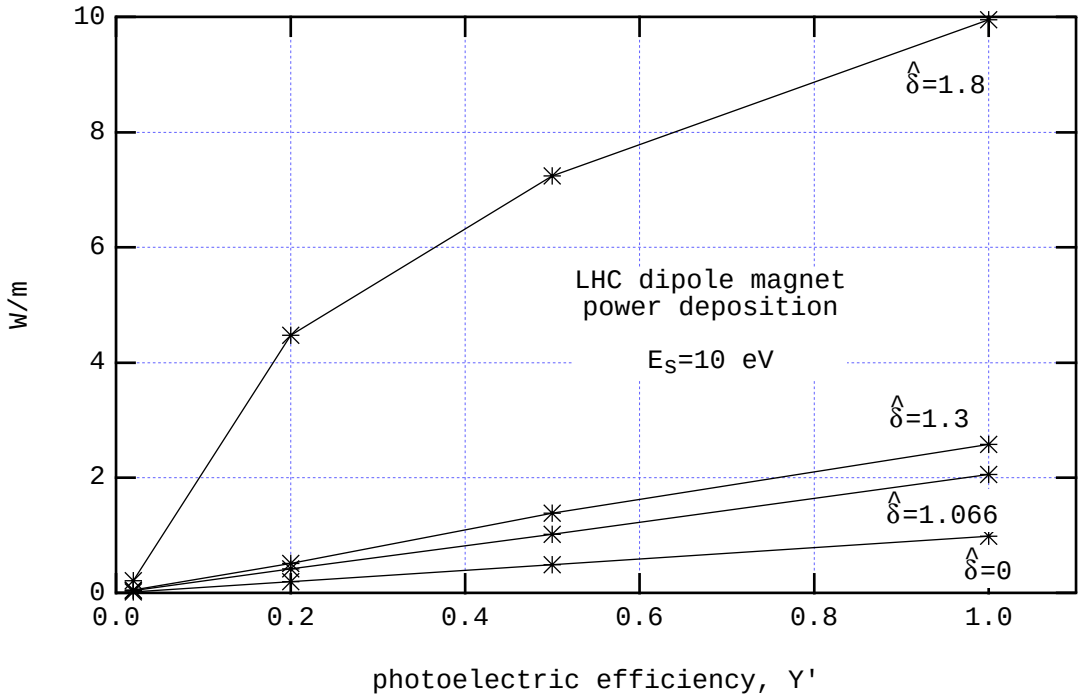

Figure 9: Power deposition per unit length in the dipole bending magnets for $E_s = 10$ eV. Other parameters are the same as those in Fig. 5.

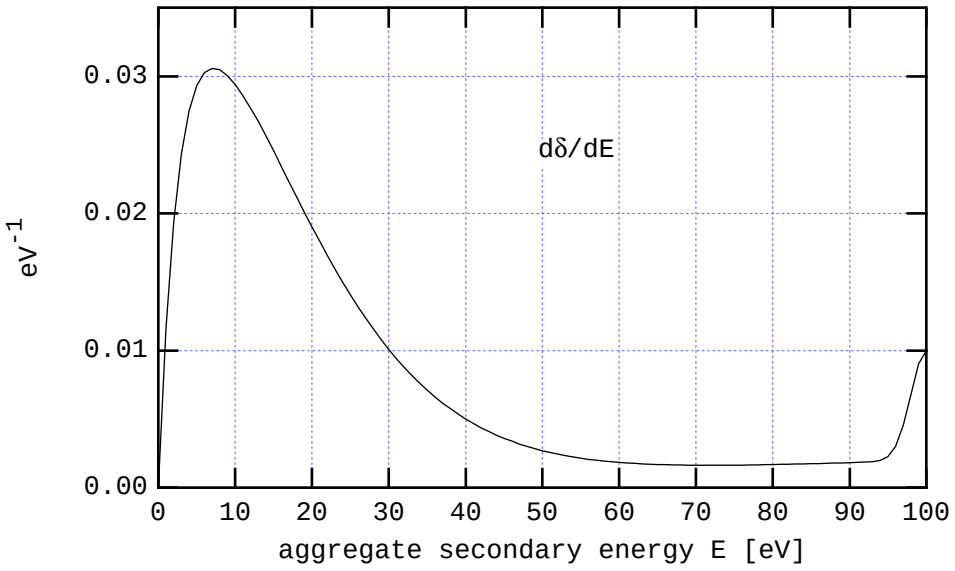

Figure 10: Energy distribution $d\delta/dE$ of emitted secondary electrons for a normally-incident electron with energy $E_0 = 100$ eV, including the elastic and rediffused components. Other parameters are the same as in Fig. 4, with which this figure should be compared.

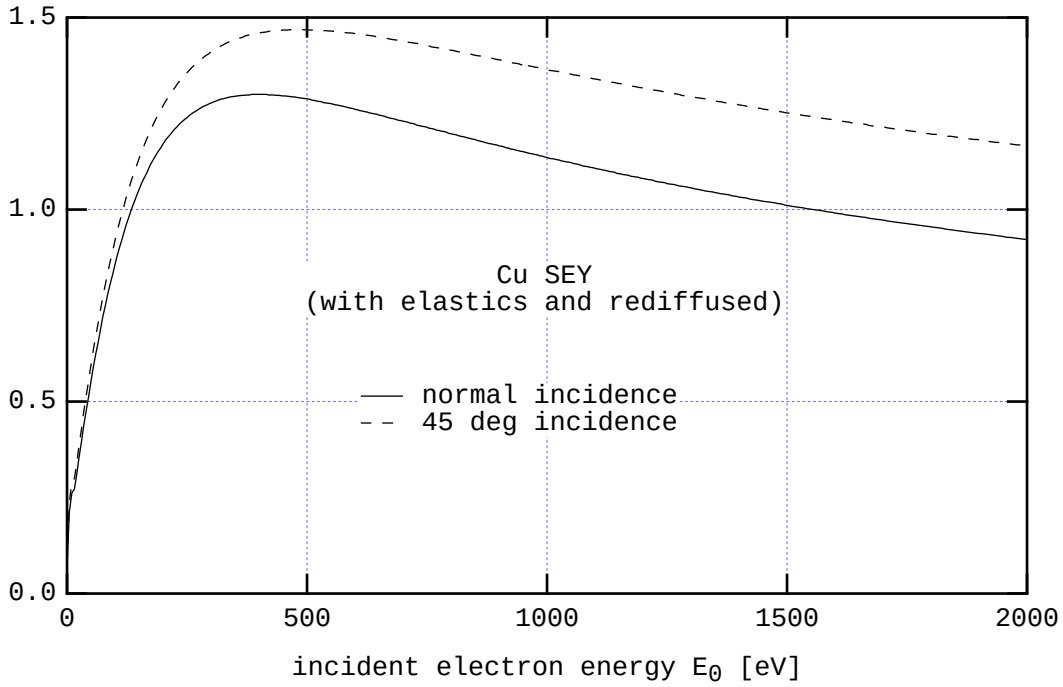

Figure 11: SEY for copper, Eqs. (16) and (17), including the elastics and rediffused components, whose parameters are described in Ref. 11. Other parameters are the same as those in Fig. 3. Comparing with this latter case, one sees an excess of electrons at low values of E_0.